Theory for Twisted Bilayer Photonic Crystal Slabs

Beicheng Lou [1,*] Nathan Zhao,[1] Momchil Minkov,[2] Cheng Guo,[1] Meir Orenstein,[3] and Shanhui Fan[2,†]

[1]*Department of Applied Physics, and Ginzton Laboratory, Stanford University, Stanford, California 94305, USA*
[2]*Department of Electrical Engineering, and Ginzton Laboratory, Stanford University, Stanford, California 94305, USA*
[3]*The Andrew and Erna Viterbi Faculty of Electrical Engineering, Technion, Haifa 32000, Israel*

We analyze scattering properties of twisted bilayer photonic crystal slabs through a high-dimensional plane wave expansion method. The method is applicable for arbitrary twist angles and does not suffer from the limitations of the commonly used supercell approximation. We show strongly tunable resonance properties of this system which can be accounted for semianalytically from a correspondence relation to a simpler structure. We also observe strongly tunable resonant chiral behavior in this system. Our work provides the theoretical foundation for predicting and understanding the rich optical physics of twisted multilayer photonic crystal systems.

In recent years, there has been a renewed interest in the rich physics that emerges when two identical lattices are stacked with a relative in-plane rotation. Depending on the twist angle, the two orientations can be commensurate, rendering the bilayer system periodic with a "supercell," or incommensurate, where the system is quasiperiodic [1]. The study of these two phases and of their interplay has recently revealed a number of novel effects in bilayer two-dimensional (2D) materials [2–15].

Photonic crystals are periodic dielectric structures that bear close analogy to periodic electronic systems [16–18]. Thus it is of interest to explore bilayer twisted photonic crystal slab structures (Fig. 1), which is a close photonic analog to twisted bilayer 2D materials. Moreover, photonic crystals have properties that are intrinsically different from their electronic counterpart [19]. While in a 2D material electrons are confined in the 2D layer, photonic crystal slabs host guided electromagnetic waves with leakage, which results in stronger interlayer interactions and allows informative probing of a system by externally incident light [20,21]. Also, compared to twisted bilayer 2D materials, twisted bilayer photonic crystal slabs allow significantly more design flexibility in terms of geometry.

In this Letter we provide a theory of light transmission and reflection through twisted bilayer photonic crystal slabs. Except for few commensurate angles, the twisted bilayer systems are quasiperiodic in general. Consequently, standard tools for the theoretical studies of photonic crystals, which rely upon the periodicity of the structure, cannot directly apply. Here we introduce the use of high-dimensional plane wave expansion into the method of rigorous coupled wave analysis (RCWA) [22,23] to treat the optical physics of twisted bilayer photonic crystal slabs. Unlike the commonly used supercell approximation [12,24], where the size of the supercell and hence the

computational cost become very large when the twisted angle is small, in our approach the computational cost is largely independent of the twisted angle, and in the small angle regime the computational cost is significantly smaller than the use of the supercell approximation. This theoretical approach enables us to explore a set of novel physical effects in such twisted bilayer systems, including the strong tunability of the transmission, reflection, chiral response, and resonant mode field distributions, as a function of the twist angle. We account for the strong tunability in terms of the moiré physics effects and by establishing a correspondence relation to a simpler structure consisting of a photonic crystal slab coupled to a uniform slab for incident light at an off-normal angle of incidence.

The exploration of moiré physics effects in photonics represents an emerging area of interest [24,25]. The physics of twisted bilayer photonic crystal slabs, which is a direct optical analog of twisted bilayer 2D materials, has not been explored prior to this work.

An example of a twisted bilayer photonic crystal slab is illustrated in Fig. 1. For each layer, a square lattice of circular holes of radius $0.25a$, where a is lattice constant, are engraved in a dielectric slab of relative permittivity $\varepsilon_r = 4$. This permittivity is representative of silicon nitride [26], which
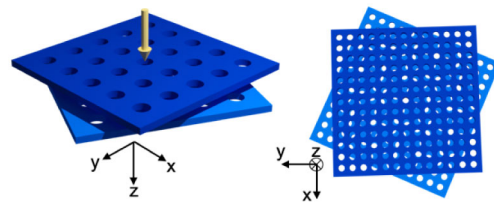

FIG. 1. Illustration of twisted bilayer photonic crystal with circular holes in a square lattice, illuminated with normally incident light.

is widely used in photonic applications [27,28]. The layer thickness is $0.2a$ and the width of the interlayer air gap is $0.3a$.

Our theoretical approach is an extension of RCWA, which has been widely used to compute the scattering properties of periodic systems. The first layer in Fig. 1 scatters an incident plane wave in air with an in-plane wave vector $\mathbf{k}_{\mathrm{inc}}$ to outgoing waves in air with in-plane wave vectors $\mathbf{k}_{\mathrm{inc}} + \mathbf{g}^{(1)}$, where $\mathbf{g}^{(i)}$ is a reciprocal lattice vector of the ith layer. This scattering process can be described as

$$b^{(1)} = \tilde{S}^{(1)}(\mathbf{k}_{\mathrm{inc}})a^{(1)}, \tag{1}$$

where $a^{(1)}$, $b^{(1)}$ are column vectors with each component being the incoming and outgoing wave field amplitudes, respectively, for each wave component with a specific in-plane wave vector as decribed above. $\tilde{S}^{(1)}(\mathbf{k}_{\mathrm{inc}})$ is the scattering matrix of the first layer, which can be routinely computed with the standard RCWA method. In typical numerical calculations, the number of reciprocal lattice vectors included can be limited to the N vectors with the smallest magnitudes. Thus, $\tilde{S}^{(1)}(\mathbf{k}_{\mathrm{inc}})$ has a dimension of $4N \times 4N$, where the factor 4 accounts for two polarizations and the upper or lower sides of the layer (more details in Supplemental Material [29], Sec. I).

We construct the scattering matrix of the twisted bilayer system, starting from the scattering matrices of the two individual layers. Below we focus on the incommensurate case. Consider the scenario discussed above, where an incident wave at $\mathbf{k}_{\mathrm{inc}}$ is scattered to a wave at $\mathbf{k}_{\mathrm{inc}} + \mathbf{g}^{(1)}$ upon transmission through the first layer. This transmitted wave is then scattered by the second layer into reflected and transmitted waves with in-plane wave vectors $\mathbf{k}_{\mathrm{inc}} + \mathbf{g}^{(1)} + \mathbf{g}^{(2)}$, in a process described by the scattering matrix $\tilde{S}^{(2)}(\mathbf{k}_{\mathrm{inc}} + \mathbf{g}^{(1)})$. The reflected wave, in turn, interacts with the first layer as described by the scattering matrix $\tilde{S}^{(1)}(\mathbf{k}_{\mathrm{inc}} + \mathbf{g}^{(1)} + \mathbf{g}^{(2)})$, and the process continues.

To describe the multiple scattering process as discussed above, it is therefore advantageous to construct two larger scattering matrices $S^{(1)}(\mathbf{k}_{\mathrm{inc}})$ and $S^{(2)}(\mathbf{k}_{\mathrm{inc}})$ of dimension $4N^2 \times 4N^2$. $S^{(1)}(\mathbf{k}_{\mathrm{inc}})$ describes the scattering process by the first layer from waves with in-plane wave vector components $\mathbf{k}_{\mathrm{inc}} + \mathbf{g}^{(1)} + \mathbf{g}^{(2)}$ to waves with $\mathbf{k}_{\mathrm{inc}} + \mathbf{g}^{(1)\prime} + \mathbf{g}^{(2)}$, for all reciprocal lattice vectors $\mathbf{g}^{(1)}$, $\mathbf{g}^{(1)\prime}$ of the first layer and $\mathbf{g}^{(2)}$ of the second layer. It is block diagonal with each block being a $\tilde{S}^{(1)}(\mathbf{k}_{\mathrm{inc}} + \mathbf{g}^{(2)})$ and thus can be constructed using the standard RCWA method applied to the first layer. $S^{(2)}(\mathbf{k}_{\mathrm{inc}})$ can be similarly defined and constructed. Once these two matrices are constructed, the scattering matrix of the bilayer system can be obtained using the same procedure as in the standard RCWA method for treating multilayer systems.

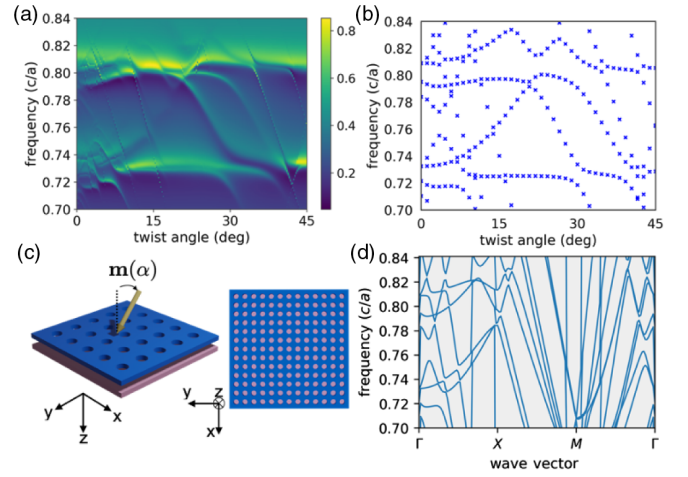The method can be extended to multilayer structures with M different twist angles by combining N^{M-1}

FIG. 2. (a) Transmission as a function of incident light frequency and twist angle for the twisted bilayer structure shown in Fig. 1. (b) Resonant frequencies of the twisted bilayer structure as a function of twist angle, as predicted from analyzing the band structure at wave vectors $\mathbf{m}(\alpha)$ of the corresponding system shown in (c). (c) The corresponding structure with one photonic crystal layer and one homogeneous layer. (d) Band structure of the corresponding structure shown in (c), with the gray background indicating the light cone.

scattering matrices into one in expanded bases for each layer. The computational cost of the algorithm scales exponentially with the number of twist angles. When combining subspace scattering matrices, various adjustments can be made. For example, at commensurate angles, plane wave bases at wave vectors $\mathbf{k}_{\mathrm{inc}} + \mathbf{g}^{(1)} + \mathbf{g}^{(2)}$ and $\mathbf{k}_{\mathrm{inc}} + \mathbf{g}^{(1)\prime} + \mathbf{g}^{(2)\prime}$ with $\mathbf{g}^{(1)} \neq \mathbf{g}^{(1)\prime}$ and $\mathbf{g}^{(2)} \neq \mathbf{g}^{(2)\prime}$ may coincide. Such a coincidence needs to be taken into account when constructing the scattering matrix.

Using the numerical techniques discussed above, we study the transmission of normally incident light through the twisted bilayer structure of Fig. 1. For normally incident plane wave, Fig. 2(a) shows the total far-field power transmission (summing all diffraction orders) of right-circularly polarized (RCP) incident light at various frequencies for twist angles from 0^+ to $45°$. The transmission features a set of resonance peaks. There are apparently two groups of resonances: one group has resonant frequencies located near 0.80 and $0.73c/a$, where c is the speed of light in vacuum; the other group has resonant frequencies strongly dependent upon the twist angle. The presence of such a twist-angle-dependent resonance is potentially interesting in practice as it highlights that the optical properties of the coupled slab system can be strongly tunable by changing the twist angle. Also, these resonances directly correlate with the poles of the transmission matrix. Thus our results show that the twist angle can be used to influence the poles of the transmission matrix as well (see Supplemental Material [29], Sec. II).

We now develop a theoretical model to account for the behaviors of both groups of resonances in the twisted photonic crystal slab structure. This model connects the behavior of the resonances of the twisted slab structure (Fig. 1) to those of a corresponding structure [Fig. 2(c)] consisting of a *single* photonic crystal slab coupled to a *uniform* slab. Specifically, we establish a *correspondence relation*: for incident light with an in-plane wave vector $\mathbf{k}_{\text{inc}}$, the resonant frequencies of a twisted bilayer system at a twist angle α can be well approximated by the resonant frequencies of the corresponding system with an in-plane wave vector,

$$\mathbf{k}_{\parallel} = \mathbf{k}_{\text{inc}} + \mathbf{m}(\alpha), \quad (2)$$

where $\mathbf{m}(\alpha) = \mathbf{g}^{(1)} - \mathbf{g}^{(2)}$ is a moiré wave vector.

We first provide a direct numerical evidence of the correspondence relation. In Fig. 2(d), we depict the band structure $\omega(\mathbf{k}_{\parallel})$ for the corresponding system. All parameters of the corresponding system are the same as for the twisted bilayer structure in Fig. 1, except that now one of the layers is replaced by a uniform dielectric slab with a relative permittivity of $\varepsilon_{\text{eff}} = 3.41$, which corresponds to the average dielectric constant of the photonic crystal slab. Here, we focus on the guided resonance modes that are concentrated in the photonic crystal slab. The band structure [Fig. 2(d)] is qualitatively very similar to that of a single photonic crystal slab [20]. In Fig. 2(b), we plot the position of the resonances in the twisted bilayer system, as predicted [33] starting from the band structure in Fig. 2(d) and using the correspondence relation Eq. (2). Comparing Figs. 2(b) and 2(a), we see that the predicted locations of the resonances match very well with the direct numerical simulations of the twisted bilayer structure. Here, to account for the main resonant features in our system, it is sufficient to take into account only the lowest-order moiré wave vectors. These wave vectors are $\mathbf{m}_{i,j}(\alpha) = \mathbf{g}_{i,j}^{(1)} - \mathbf{g}_{i,j}^{(2)}$, where $(i,j) \in \{(0,1), (1,0), (0,-1), (-1,0)\}$, and $\mathbf{g}_{i,j}^{(n)} = (i \cdot \hat{\mathbf{x}}^{(n)} + j \cdot \hat{\mathbf{y}}^{(n)})2\pi/a$, with $\hat{\mathbf{x}}^{(n)}$ and $\hat{\mathbf{y}}^{(n)}$ being the unit vectors along the [10] and [01] directions of the nth layer.

We now provide a justification of the correspondence relation discussed above. The modes of this system in general can be obtained by solving an eigenvalue problem:

$$\hat{H}|\psi\rangle = \left(\frac{\omega^2}{c^2}\right)|\psi\rangle, \quad (3)$$

where $\hat{H} = \nabla \times [1/\epsilon(\mathbf{r})]\nabla\times$ is the effective Hamiltonian with $\epsilon(\mathbf{r})$ being the spatial distribution of the electric permittivity and $|\psi\rangle$ denoting the magnetic field distribution of the eigenmodes [34]. As a good approximation, we can expand the eigenmodes on the basis of

$$|\mathbf{k}_{\text{inc}} + \mathbf{g}^{(1)} + \mathbf{g}^{(2)}\rangle_i \equiv \phi_i(z)e^{-i(\mathbf{k}_{\text{inc}}+\mathbf{g}^{(1)}+\mathbf{g}^{(2)})\cdot\mathbf{r}_{\parallel}}, \quad (4)$$

where $i = 1, 2$ labels the two layers, $\mathbf{r}_{\parallel}$ denotes the in-plane coordinates, and $\phi_i(z)$ is the profile along the z direction of

the guided mode for the ith layer. We use $\hat{H}(\mathbf{k}_{\text{inc}})$ to denote the matrix obtained by projecting the Hamiltonian on this basis set. The choices of the in-plane wave vectors in this basis set represent all possible in-plane wave vectors which the incident wave can scatter into. Thus, the eigenstates for the matrix $\hat{H}(\mathbf{k}_{\text{inc}})$ describe all possible guided resonances that the incident wave can couple into.

In the following, we will prove that $\hat{H}(\mathbf{k}_{\text{inc}})$ for the twisted bilayer system can be approximated by a block-diagonal matrix, which describes the modes of the corresponding system at $\mathbf{k}_{\text{inc}} + \mathbf{m}(\alpha)$. We focus on the general case where the twist angle α is incommensurate. Since $\mathbf{g}^{(2)} = \mathbf{g}^{(1)} + \mathbf{m}(\alpha)$, we can equivalently write each of the basis states in Eq. (4) as $|\mathbf{k}_{\text{inc}} + \mathbf{m}(\alpha) + \mathbf{g}^{(1)}\rangle_i$. Consider a basis state $|\mathbf{k}_{\text{inc}} + \mathbf{m}(\alpha) + \mathbf{g}^{(1)}\rangle_1$ confined in the first layer. Among all the states $|\mathbf{k}_{\text{inc}} + \mathbf{m}'(\alpha) + \mathbf{g}^{(1)\prime}\rangle_1$ confined in the first layer, this state will dominantly couple to the states with $\mathbf{m}' - \mathbf{m}$ being a reciprocal lattice vector of the first layer, since the coupling is facilitated by the periodic dielectric variation in the first layer. In contrast, to a state where $\mathbf{m}' - \mathbf{m}$ is not a reciprocal lattice vector of the first layer, the coupling is significantly weaker, since in this case it must be facilitated by the periodic dielectric variation of the second layer, which has a much weaker overlap with $\phi_1(z)$. Similarly, to a basis state $|\mathbf{k}_{\text{inc}} + \mathbf{m}'(\alpha) + \mathbf{g}^{(1)\prime}\rangle_2$ that is confined in the second layer, the coupling from $|\mathbf{k}_{\text{inc}} + \mathbf{m}(\alpha) + \mathbf{g}^{(1)}\rangle_1$ is also significantly weaker, since the coupling strength involves an overlap integral of $\phi_1(z)$ and $\phi_2(z)$, which are spatially separated.

Therefore, $\hat{H}(\mathbf{k}_{\text{inc}})$ can be approximated as a block-diagonal matrix, with each block describing the coupling among the basis states $|\mathbf{k}_{\text{inc}} + \mathbf{m}(\alpha) + \mathbf{g}^{(1)}\rangle_i$ due to dielectric distribution within the ith layer. As seen from Eq. (3), the coupling between $|\mathbf{k}_{\text{inc}} + \mathbf{m}(\alpha) + \mathbf{g}^{(1)}\rangle_1$ and $|\mathbf{k}_{\text{inc}} + \mathbf{m}(\alpha) + \mathbf{g}^{(1)\prime}\rangle_1$ involves the contributions from the dielectric permittivity of both slabs. However, since the angle α is incommensurate, the permittivity of the second slab cannot facilitate the coupling between these two states with $\mathbf{g}^{(1)} \neq \mathbf{g}^{(1)\prime}$. Therefore, for incident light with an in-plane wave vector $\mathbf{k}_{\text{inc}}$, the modes in the twisted bilayer that are excited can be well described by the modes of a single photonic crystal slab coupled to a uniform dielectric slab with incident in-plane wave vector at $\mathbf{k}_{\text{inc}} + \mathbf{m}(\alpha)$. We have therefore provided a justification of the correspondence relation.

The correspondence relation provides an understanding of the origin of different angle dependencies of the resonances as observed in Fig. 2(a). In the case of Fig. 2(a), $\mathbf{k}_{\text{inc}} = 0$. For the corresponding structure shown in Fig. 2(c), the resonant frequencies at the wave vector $\mathbf{m}(\alpha)$ are in the vicinity of

$$\omega_{i,j}^{(1)} = \frac{c}{\sqrt{\varepsilon_{\text{eff}}}}|\mathbf{m}(\alpha) + \mathbf{g}_{i,j}^{(1)}|. \quad (5)$$
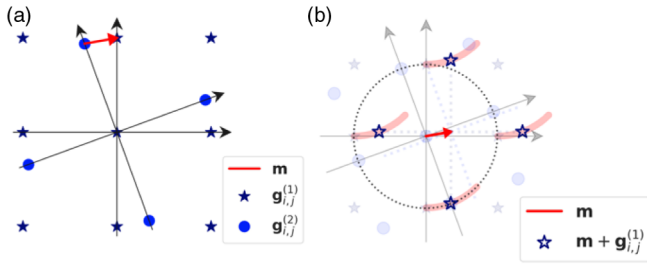
FIG. 3. (a) The blue circles and stars denote the reciprocal lattices of the two layers, respectively. The red arrow is one of the first-order moiré wave vectors. (b) Illustration of in-plane wave vectors (open stars) of the basis functions of the Hamiltonian in Eq. (3), with the twist angle dependence shown in red shades. The dotted circle is the unit circle.
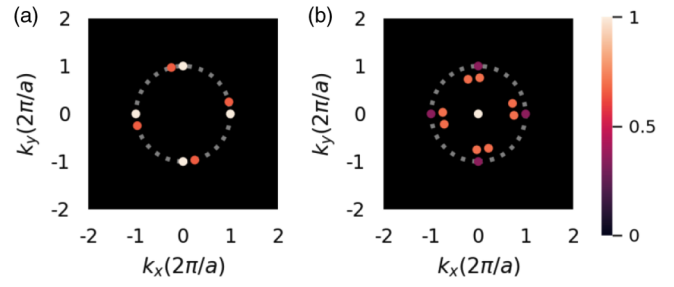

FIG. 4. The magnitude of the electric field distribution immediately below the bottom layer in wave vector space for (a) a twist-angle-independent resonance and (b) a twist-angle-dependent resonance. The dotted circles are the unit circles.

For every $\mathbf{m}(\alpha)$, there is in fact a choice of $\mathbf{g}_{i,j}^{(1)}$ for which $\omega_{i,j}^{(1)}$ is independent of the twist angle α. Here in Fig. 3 we provide an illustration. Consider the case where $\mathbf{m}(\alpha) = \mathbf{g}_{0,1}^{(1)} - \mathbf{g}_{0,1}^{(2)}$ [red arrow in Fig. 3(a)]. As α varies, $\mathbf{m}(\alpha) + \mathbf{g}_{0,-1}^{(1)}$ moves on a circle [dotted circle in Fig. 3(b), denoted as the *unit circle*] centered at the origin in wave vector space with a radius of $|\mathbf{g}_{0,1}^{(1)}|$. Thus, the corresponding resonant frequency in the twisted bilayer system is largely independent of the twist angle. In contrast, the resonances in the twisted bilayer system that correspond to $\mathbf{g}_{0,1}^{(1)}$, $\mathbf{g}_{\pm1,0}^{(1)}$ under this specific choice of $\mathbf{m}(\alpha)$ have strong angle dependency, since for each of these cases $\mathbf{m}(\alpha) + \mathbf{g}_{i,j}^{(1)}$ does not stay on the unit circle as α varies, and instead $|\mathbf{m}(\alpha) + \mathbf{g}_{i,j}^{(1)}|$ become α dependent, as also shown in Fig. 3(b).

Our understanding of the resonant modes can be confirmed by the field distribution near the structure as excited by the incident plane wave. Figure 4 compares the wave-vector-space distributions of the magnitude of the electric field $|E|$ on a plane immediately beneath the bottom layer at a twist angle $\alpha = 14.32°$ for two different resonances (with real-space distributions and other examples in Supplemental Material [29], Sec. III). For the twist-angle-independent resonance [Fig. 4(a)], the field is distributed primarily on the unit circle. For the twist-angle-dependent resonance [Fig. 4(b)], the dominant peaks are within the unit circle. These distributions are consistent with our discussion above on the correspondence relation.

The bilayer system considered here is chiral. The bilayer system at an incommensurate twist angle has C_4 symmetry. Thus, for the normally incident light, the spin of the photons is preserved in the zeroth-order diffraction process. [The spin of ±1 corresponds to RCP and left-circularly polarized (LCP) light, respectively.] Since the twisted bilayer system in general does not have mirror symmetry, the responses of the system to RCP and LCP incident light

are different. In Fig. 5(a), we consider the total transmission T_{RCP} and T_{LCP} for RCP and LCP incident light, respectively. We plot normalized transmission contrast $(T_{\mathrm{RCP}} - T_{\mathrm{LCP}})/(T_{\mathrm{RCP}} + T_{\mathrm{LCP}})$ as a function of frequency and twist angle. The magnitude of such contrast gives a measure of the strength of the chiral response of the system.

Examining Fig. 5(a), we note that the chiral response is prominent only at the resonances of the system. This is expected since the direct scattering process [20] consists of transmission through the effective uniform slabs, which is not chiral. The chiral response has an odd symmetry along the angle axis with respect to 0 and 45°, as can be understood by the transformation of the twist angle with respect to the mirror plane at these angles. The chiral response vanishes at $\alpha = 0°$ or 45°, where the bilayer structure has C_{4v} symmetry.

In Fig. 5(a), we also note that the chiral response is significantly weaker in the region between the lines of $\omega = 2\sin(\alpha/2)2\pi c/a$ and $\omega = 2\sin[(\pi/2 - \alpha)/2]2\pi c/a$, shown as the red dashed lines in Fig. 5(a), in spite of the fact that there are prominent resonances in this region, as can be seen by examining Fig. 2(a). Below, we refer to these lines as the *moiré light line*. This effect can be
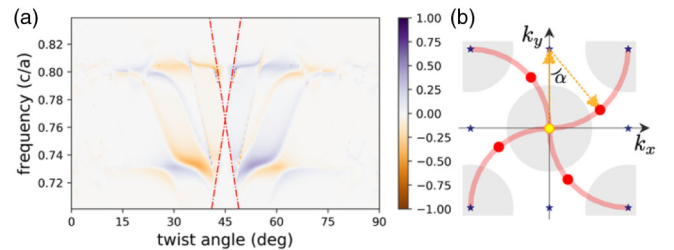

FIG. 5. (a) $(T_{\mathrm{RCP}} - T_{\mathrm{LCP}})/(T_{\mathrm{RCP}} + T_{\mathrm{LCP}})$ as a function of frequency and twist angle. The moiré light line is marked by red dashed lines. (b) Illustration of the lowest-order scattering process that contributes to the chiral responses. The stars represent the reciprocal lattice of the first layer. The gray regions indicate the light cone. The red circles represent the relevant moiré wave vectors $\mathbf{m}(\alpha)$, with the twist angle dependence captured by the red shades. The intersections between the red shades and the gray regions are on the moiré light line.

understood as follows: the lowest-order scattering process that contributes to the chiral response consists of the normally incident plane wave being scattered by the first layer to the states with small wave vectors such as $\mathbf{g}_{0,1}^{(1)}$, which are then scattered by the second layer to wave components in free space with small in-plane wave vectors such as $\mathbf{g}_{0,1}^{(1)} - \mathbf{g}_{0,1}^{(2)}$ [Fig. 5(b), orange arrows]. These wave components transition between being evanescent and being propagating at the moiré light lines. Between the moiré light lines, the chiral transmission contrast is weaker since these wave components are evanescent along the z direction and do not contribute to the chiral transmission contrast which arises only from the propagating field.

The behavior at this moiré light line, where a diffraction order transitions from being evanescent to being propagating, is reminiscent of Wood's anomaly in grating structures [35,36]. In standard grating structures or photonic crystal slabs, the effects of Wood's anomaly manifest as one varies the frequency or the angle of the incident light. In contrast, in the bilayer system here, the Wood's anomaly can in addition be probed by varying the twist angle.

To summarize, we have presented a theoretical analysis of twisted bilayer photonic crystal slabs. Our work provides a theoretical foundation for understanding the very rich set of optical physics of twisted bilayer photonic crystal slab systems. Such understanding may prove useful in developing tunable filters, lasers, and optomechanical devices.

---

[*]beichenglou@stanford.edu

[†]shanhui@stanford.edu

[1] C. Janot, *Quasicrystals: A Primer*, Monographs on the Physics and Chemistry of Materials, 2nd ed. (Oxford University Press, Oxford, 2012).

[2] Y. Cao, V. Fatemi, S. Fang, K. Watanabe, T. Taniguchi, E. Kaxiras, and P. Jarillo-Herrero, Unconventional superconductivity in magic-angle graphene superlattices, Nature (London) **556,** 43 (2018).

[3] Y. Xie, B. Lian, B. Jäck, X. Liu, C.-L. Chiu, K. Watanabe, T. Taniguchi, B. A. Bernevig, and A. Yazdani, Spectroscopic signatures of many-body correlations in magic-angle twisted bilayer graphene, Nature (London) **572,** 101 (2019).

[4] M. Yankowitz, S. Chen, H. Polshyn, Y. Zhang, K. Watanabe, T. Taniguchi, D. Graf, A. F. Young, and C. R. Dean, Tuning superconductivity in twisted bilayer graphene, Science **363,** 1059 (2019).

[5] Y. Cao, V. Fatemi, A. Demir, S. Fang, S. L. Tomarken, J. Y. Luo, J. D. Sanchez-Yamagishi, K. Watanabe, T. Taniguchi, E. Kaxiras *et al.*, Correlated insulator behaviour at half-filling in magic-angle graphene superlattices, Nature (London) **556,** 80 (2018).

[6] Z. Bi, N. F. Q. Yuan, and L. Fu, Designing flat bands by strain, Phys. Rev. B **100,** 035448 (2019).

[7] H. P. Büchler, G. Blatter, and W. Zwerger, Commensurate-Incommensurate Transition of Cold Atoms in an Optical Lattice, Phys. Rev. Lett. **90,** 130401 (2003).

[8] C. R. Woods, L. Britnell, A. Eckmann, R. S. Ma, J. C. Lu, H. M. Guo, X. Lin, G. L. Yu, Y. Cao, R. V. Gorbachev, A. V. Kretinin, J. Park, L. A. Ponomarenko, M. I. Katsnelson, Y. N. Gornostyrev, K. Watanabe, T. Taniguchi, C. Casiraghi, H. J. Gao, A. K. Geim, and K. S. Novoselov, Commensurate-incommensurate transition in graphene on hexagonal boron nitride, Nat. Phys. **10,** 451 (2014).

[9] C. R. Dean, L. Wang, P. Maher, C. Forsythe, F. Ghahari, Y. Gao, J. Katoch, M. Ishigami, P. Moon, M. Koshino *et al.*, Hofstadters butterfly and the fractal quantum Hall effect in moiré superlattices, Nature (London) **497,** 598 (2013).

[10] J. Liu, Z. Ma, J. Gao, and X. Dai, Quantum Valley Hall Effect, Orbital Magnetism, and Anomalous Hall Effect in Twisted Multilayer Graphene Systems, Phys. Rev. X **9,** 031021 (2019).

[11] S. Huang, K. Kim, D. K. Efimkin, T. Lovorn, T. Taniguchi, K. Watanabe, A. H. MacDonald, E. Tutuc, and B. J. LeRoy, Topologically Protected Helical States in Minimally Twisted Bilayer Graphene, Phys. Rev. Lett. **121,** 037702 (2018).

[12] S. S. Sunku, G. X. Ni, B. Y. Jiang, H. Yoo, A. Sternbach, A. S. McLeod, T. Stauber, L. Xiong, T. Taniguchi, K. Watanabe, P. Kim, M. M. Fogler, and D. N. Basov, Photonic crystals for nano-light in moiré graphene superlattices, Science **362,** 1153 (2018).

[13] T. Stauber, T. Low, and G. Gómez-Santos, Chiral Response of Twisted Bilayer Graphene, Phys. Rev. Lett. **120,** 046801 (2018).

[14] Z. Wu, X. Chen, M. Wang, J. Dong, and Y. Zheng, High-performance ultrathin active chiral metamaterials, ACS Nano **12,** 5030 (2018).

[15] Z. Wu and Y. Zheng, Moir chiral metamaterials, Adv. Opt. Mater. **5,** 1700034 (2017).

[16] S. John, Strong Localization of Photons in Certain Disordered Dielectric Superlattices, Phys. Rev. Lett. **58,** 2486 (1987).

[17] J. D. Joannopoulos, P. R. Villeneuve, and S. Fan, Photonic crystals: Putting a new twist on light, Nature (London) **386,** 143 (1997).

[18] E. Yablonovitch, Inhibited Spontaneous Emission in Solid-State Physics and Electronics, Phys. Rev. Lett. **58,** 2059 (1987).

[19] T. Ozawa, H. M. Price, A. Amo, N. Goldman, M. Hafezi, L. Lu, M. C. Rechtsman, D. Schuster, J. Simon, O. Zilberberg, and I. Carusotto, Topological photonics, Rev. Mod. Phys. **91,** 015006 (2019).

[20] S. Fan and J. D. Joannopoulos, Analysis of guided resonances in photonic crystal slabs, Phys. Rev. B **65,** 235112 (2002).

[21] C. Guo, M. Xiao, Y. Guo, L. Yuan, and S. Fan, Meron Spin Textures in Momentum Space, Phys. Rev. Lett. **124,** 106103 (2020).

[22] M. G. Moharam, E. B. Grann, D. A. Pommet, and T. K. Gaylord, Formulation for stable and efficient implementation of the rigorous coupled-wave analysis of binary gratings, J. Opt. Soc. Am. A **12**, 1068 (1995).

[23] V. Liu and S. Fan, S^4: A free electromagnetic solver for layered periodic structures, Comput. Phys. Commun. **183**, 2233 (2012).

[24] P. Wang, Y. Zheng, X. Chen, C. Huang, Y. V. Kartashov, L. Torner, V. V. Konotop, and F. Ye, Localization and delocalization of light in photonic Moiré lattices, Nature (London) **577**, 42 (2020).

[25] G. Hu, Q. Ou, G. Si, Y. Wu, J. Wu, Z. Dai, A. Krasnok, Y. Mazor, Q. Zhang, Q. Bao, C.-W. Qiu, and A. Alù, Topological polaritons and photonic magic angles in twisted α-MoO$_3$ bilayers, Nature (London) **582**, 209 (2020).

[26] H. Philipp, Silicon nitride (Si$_3$N$_4$) (noncrystalline), in *Handbook of Optical Constants of Solids*, edited by E. D. Palik (Academic Press, Burlington, VT, 1997), pp. 771–774.

[27] D. J. Blumenthal, R. Heideman, D. Geuzebroek, A. Leinse, and C. Roeloffzen, Silicon nitride in silicon photonics, Proc. IEEE **106**, 2209 (2018).

[28] L. Vogelaar, W. Nijdam, H. A. G. M. van Wolferen, R. M. de Ridder, F. B. Segerink, E. Flck, L. Kuipers, and N. F. van Hulst, Large area photonic crystal slabs for visible light with waveguiding defect structures: Fabrication with focused ion beam assisted laser interference lithography, Adv. Mater. **13**, 1551 (2001).

[29] See Supplemental Material at http://link.aps.org/supplemental/10.1103/PhysRevLett.126.136101 for more details on (1) the numerical method, (2) the zero/pole structures in the scattering matrix, and (3) the steady-state field distributions, which includes Refs. [30–32].

[30] L. Li, New formulation of the Fourier modal method for crossed surface-relief gratings, J. Opt. Soc. Am. A **14**, 2758 (1997).

[31] M. Born, E. Wolf, A. B. Bhatia, P. C. Clemmow, D. Gabor, A. R. Stokes, A. M. Taylor, P. A. Wayman, and W. L. Wilcock, *Principles of Optics: Electromagnetic Theory of Propagation, Interference and Diffraction of Light*, 7th ed. (Cambridge University Press, Cambridge, England, 1999).

[32] A. Y. Song, A. R. K. Kalapala, W. Zhou, and S. Fan, First-principles simulation of photonic crystal surface-emitting lasers using rigorous coupled wave analysis, Appl. Phys. Lett. **113**, 041106 (2018).

[33] M. Minkov, I. A. D. Williamson, L. C. Andreani, D. Gerace, B. Lou, A. Y. Song, T. W. Hughes, and S. Fan, Inverse design of photonic crystals through automatic differentiation, ACS Photonics **7**, 1729 (2020).

[34] J. D. Joannopoulos, S. G. Johnson, J. N. Winn, and R. D. Meade, *Photonic Crystals: Molding the Flow of Light*, 2nd ed. (Princeton University Press, Princeton, NJ, 2008).

[35] R. W. Wood, On a remarkable case of uneven distribution of light in a diffraction grating spectrum, Proc. Phys. Soc. London **18**, 269 (1902).

[36] A. Hessel and A. A. Oliner, A new theory of woods anomalies on optical gratings, Appl. Opt. **4**, 1275 (1965).